Search for shallow subsurface structures in Chryse and Acidalia Planitiae on Mars

Aina Oura [1], Kasaba Yasumasa [1], Rina Noguchi [2], Atsushi Kumamoto [3], Ken Ishiyama [4], Tomohiro Usui [2], Fuminori Tsuchiya [1], Chihiro Uemura [5], Tomoki Kimura [3]

[1] Planetary Plasma and Atmospheric Research Center, Tohoku University, Aramaki-Aza-Aoba 6-3, Aoba-ku, Sendai, Miyagi 980-8578, Japan

[2] Institute of Space and Astronautical Science, Japan Astronautical Exploration Agency, 3-1-1 Yoshinodai, Sagamihara, Kanagawa 252-5210, Japan

[3] Department of Geophysics, Tohoku University, Aramaki-Aza-Aoba 6-3, Aoba-ku, Sendai, Miyagi 980-8578, Japan

[4] National Institute of Technology Tsuruoka College, 104 Sawada, Inooka, Tsuruoka, Yamagata 997-8511, Japan

[5] SOKENDAI (Graduate University for Advanced Studies), 3-1-1 Yoshinodai, Chuo-ku, Sagamihara, Kanagawa 252-5210, Japan

Corresponding author: Aina Oura (oura.a@pparc.gp.tohoku.ac.jp)

Key Points:

- We found subsurface reflectors at 22 locations across Chryse and Acidalia Planitiae. They do not construct wide subsurface structures.
- The dielectric constants at two locations constrained the porosity and the upper limit for the volume fraction of water ice.
- The estimated porosities of the shallow subsurface layers correspond to those of basaltic rock or till.

Abstract

We surveyed the subsurface structure of Chryse and Acidalia Planitiae using data from the Mars SHAllow RADar sounder (SHARAD) onboard the Mars Reconnaissance Orbiter (MRO). Several subsurface reflectors were identified in these regions, but these reflectors do not constitute apparent subsurface structures larger than 30 km. The bulk dielectric constants of the uppermost layers at two locations were estimated as 5.3 and 5.9 from the combination of high-resolution images and topographic data. These values were used to constrain the possible bulk porosity (approximately 28 % and 25 %) and the upper limit for the volume fraction of water ice (~43 % and ~50 %). The estimated porosities of the shallow subsurface layers in these locations can be explained by the emplacement of basaltic rock or till that may contain some ice-cemented regolith.

Plain Language Summary

We explored the subsurface structure on Mars using radar sounding data combined with high-resolution images and topographic data. We identified scattered reflectors in Chryse and Acidalia Planitiae, but these reflectors do not appear to constitute subsurface structures. The estimated dielectric constants at two locations were 5.3 and 5.9. These values constrained the bulk porosity (~28 % and ~25 %) and the upper limit for the volume fraction of water ice (~43 % and ~50 %). The expected bulk porosity agreed that the uppermost layers of these locations could be basaltic rock or till.

1 Introduction

Recently, studies have been conducted investigating the mid-latitude subsurface ice (e.g., discoveries of exposed ice sheets [Dundas et al., 2018] and the widespread presence of excess ice [Bramson et al., 2015]). New discoveries of Martian ice are attributed to high resolution visible images, spectrum and/or radar sounding data. Previous research identified the 1.2×10^6 km^2 area in Arcadia Planitia and the 3.75×10^5 km^2 area in Utopia Planitia that are covered by ice (Bramson et al., 2015; Stuurman et al., 2016). However, mid-latitude water ice is currently unstable, as implied by climate models (Schorghofer and Aharonson, 2005). This controversy could be attributed to the high obliquity of Mars, as it is possible that this obliquity may lead to ice being carried from the polar caps to the mid-latitudes, where it is preserved as subsurface ice (Jakosky and Carr., 1985). Information about the subsurface structure, and especially underground ice, at mid-latitudes is therefore required to investigate this explanation for the presence of current mid-latitude ice. This study is therefore focused on identifying the subsurface structures in Chryse and Acidalia Planitiae (CAP).

The CAP regions are northern plains at which subsurface structures have not yet been detected by radar sounding. One of the unique aspects of CAP is the presence of many Recurring Slope Lineae (RSL) (Stillman et al., 2016), which are characterized by narrow dark features that lengthen incrementally in a downwards direction on steep slopes, fade in colder seasons, and recur annually. The origin of RSL is still under debate, with dry granular or briny water flows still discussed (Huber et al., 2020). Candidate and confirmed RSL sites are mainly distributed over four regions: the southern mid-latitudes (SML), Valles Marineris (VM), the equatorial highlands, and Chryse and Acidalia Planitiae (Stillman et al., 2016). The RSL of VM and CAP are denser than those observed in other locations. As CAP are wide plains that reduce off-nadir

surface echoes, it is preferable that the subsurface structure is more easily investigated by radar sounding.

The CAP regions have experienced volcanism (Head et al., 2002), sedimentary deposition (Kreslavsky and Head, 2002), and the effects of recent climate change (Mustard et al., 2001; Costard et al., 2002). These regions are characterized by abundant outflow channels that are thought to have been excavated by erosion resulting from catastrophic floods (Rodoriguez et al., 2014), glaciers (Pacifici et al., 2009; Rodoriguez et al., 2014), CO_2-charged debris flows (Hoffman, 2000), H_2O-charged debris flows (Tanaka, 1999; Rodriguez et al., 2006), and/or lava flows (Leverington, 2011). Whether these materials were emplaced on a standing body of water (Baker et al., 1991), as an ice-dominated unit (Carr, 1996; Clifford and Parker, 2001), or as sediment-dominated effluents (Kreslavsky and Head, 2002) has additional implications regarding the modification of the northern plains during the period between the late Hesperian and/or the early Amazonian.

This study is a survey of the subsurface structures in the CAP regions with the objective of clarifying the relationship between the subsurface structures and the geologic or topographic features (e.g., RSL and outflow channels). Data from the Mars SHAllow RADar sounder (SHARAD, Seu et al., 2007) onboard the Mars Reconnaissance Orbiter (MRO) were utilized, combined with high-resolution images and topographic data. The bulk dielectric constants of the uppermost layers were estimated using the exposed stratigraphy. We then discuss the materials deposited in CAP according to the results of component calculations.

2 Methods

SHARAD gathers data over frequencies from 15 to 25 MHz with a bandwidth of 10 MHz, providing a vertical resolution of 15 m in a vacuum and approximately 8 m in water ice. The spatial resolution is 0.3 to 1 km along the track and 3 to 6 km along the cross-track direction (Seu et al., 2007).

The CAP region was surveyed using 217 SHARAD data that were provided by the Geosciences node of the Planetary Data System (PDS), which cover the area lying approximately 19.5°N – 40°N, and from -55°E to -27°E, in order to examine the distribution of the subsurface reflectors. Subsurface reflectors were identified at a resolution of 0.05° (approximately 3 km) along the track. The Hann weighting function was applied to the data for ground processing, and first and second sidelobes were expected with delays of 240 and 420 ns (Putzig et al., 2014). Considering the delay time of the sidelobes, we divided the subsurface reflectors into five categories (0–220, 220–260, 260–400, 400–440, and 440–3000 ns), and converted the delay time in the radar data to the apparent elevation assumed in a vacuum in order to generate radargrams. The radargrams usually contain off-nadir surface echoes known as ‘clutter’, which have a similar delay time to the subsurface echoes. For the rejection of clutter echoes, we generated simulated radargrams using the Kirchhoff Approximation Method based on the Mars Orbiter Laser Altimeter (MOLA, Smith et al., 2001) -derived digital elevation model (https://pds-geosciences.wustl.edu/mgs/mgs-m-mola-5-megdr-l3-v1/mgsl_300x/meg128/) as given by Text S2 of Noguchi et al. (2020). By comparing the observed radargrams with the simulated ones, the clutter signals could be removed from the observed radargrams and the subsurface reflectors were identified. We then obtained the 2-way time delay (Δt) and mapped the locations of subsurface reflectors using QGIS (version 3.6).

Using the same method as Noguchi et al. (2020), we also searched the exposed crater walls close to the candidate reflectors using the images from High Resolution Imaging Science Experiment (HiRISE) (McEwen et al., 2007). The depth (d) of the identified layers was measured from the HiRISE digital terrain models (HiRISE DTMs) produced by MarsSI (https://marssi.univ-lyon1.fr/MarsSI/) (Quantin-Nataf et al., 2018). Three HiRISE DTMs were available for the CAP regions (**Figs. 1 and S1**). The procedure used by MarsSI is: 1) the HiRISE EDR images are imported (raw data) and calibrated, 2) the DTMs are created, and 3) the DTMs are aligned with the data produced by MOLA. The stratigraphic columns were then generated using StratGen (version 1.6.0), which is produced by the Indiana Geological Survey at Indiana University, and the layers were classified into three types according to appearance: fine, coarse, and very coarse (Noguchi et al., 2020). The fine layers contain no obvious boulders/rocks, very coarse layers appear similar to fractured lava or boulder-rich rocks, and the coarse layers have an intermediate appearance between the fine and the very coarse layers.

The plausible dielectric constant (ε_{bulk}) can be derived from a combination of the 2-way time delay in the radargram and the depth to the identified layer (d), using the equation:

$$d = \frac{\Delta t}{2} \times \frac{c}{\sqrt{\varepsilon_{bulk}}}$$

where c is the speed of light in a vacuum (3.0×10^8 m/s). The dielectric constant of a mixture of rocks, vacuum, and water ice is given by:

$$\varepsilon_{bulk} = \varepsilon_{vacuum} + \frac{3b}{1-b}\varepsilon_{vacuum}$$

$$b = \phi_{ice}\frac{\varepsilon_{ice} - \varepsilon_{vacuum}}{\varepsilon_{ice} - \varepsilon_{vacuum}} + \phi_{rock}\frac{\varepsilon_{rock} - \varepsilon_{vacuum}}{\varepsilon_{rock} - \varepsilon_{vacuum}}$$

where ε_{vacuum}, ε_{rock}, and ε_{ice} are the dielectric constants of vacuum, rock, and water ice, respectively (Ishiyama et al., 2019). The volume fractions of rock and ice in a target layer are depicted as ϕ_{rock} and ϕ_{ice}, respectively. In this study, we applied ε_{vacuum} = 1, ε_{ice} = 3.15 (Matsuoka et al., 1997), and ε_{rock} = 14.9 (Rust et al., 1999) based on Noguchi et al. (2020). We also show the results of a component calculation for situations in which the dielectric constant of non-porous rock is 8 in the supplementary information **Text S3** so that the results can be compared with previous studies. The probable materials comprising the uppermost layers were estimated using these equations and parameters.

Figure 1. Surveyed outcrops and their interpreted stratigraphic columns. (A) and (B) are two HiRISE DTMs in the CAP regions derived from MarsSI. The locations are shown in **Fig. 3**. (A) is DTM-[A] (HI_052222_2070_053079_2070-ALIGN-DRG). (B) is DTM-[B] (HI_003222_2055_018834_2060-ALIGN-DRG). Light blue arrows show the locations of the exposed stratigraphy. (C) and (D) are the stratigraphic columns at each location. (C) is derived from DTM-[A] and (D) is derived from DTM-[B].

3 Results

A total of 22 locations of scattered subsurface reflectors were found in the CAP regions (**Fig. 2**). The average delay time of the subsurface reflectors differed from the delay time of the sidelobes (220–260 ns and 400–440 ns). The reflectors on the MRO footprint were at least 6 km

in length, reaching a maximum of 15 km, and were spread over a wide area (15–350 km). Seven subsurface reflectors were located near the mouths of outflow channels, as seen in **Fig. 2**. These reflectors are short on the footprint (at 9 km or less) and are isolated at 25 km or more apart. In addition, we noticed subsurface reflectors were located near the rampart craters. The closest distance between the rampart crater and subsurface reflectors was 15 km, as shown in **Fig. 2**.

In order to investigate the structure of the layers in the subsurface, the exposed stratigraphy in the selected area was drawn using two HiRISE DTMs (**Fig. 1)**. This area of interest (AOI: approximately 22°N – 33°N and from -47.5°E to -37.5°E in **Fig. 2**) covers several geological units (**Fig. 3**). The reflectors in the AOI are relatively close together (25–170 km) compared to the rest of the identified reflectors. The two HiRISE DTMs and the seven subsurface reflectors (labeled **(a)**, **(b)-1**, **(b)-2**, **(c)**, **(e)**, **(f)** and **(h)**) were located on the same unit, AHcs (Smooth unit, **Text S1**); we therefore assumed that these reflectors potentially represent a common subsurface structure that is linked to this unit. Furthermore, the stratigraphy comprising both of the subsurface layers is exposed on the inner wall of the two DTMs because craters of this size are deep enough for the subsurface structure to be observed. We therefore used the method in which the bulk dielectric constants in this part of the AOI are calculated. The candidate reflectors on the AHcs unit were less than 200 km apart, while the adjacent footprints of the MRO surveyed in this study were at least 1.5 km apart, reaching a maximum distance of 30 km. Thus, our results do not support the presence of wide subsurface materials with large permittivity contrasts that reach sizes of more than 30 km.

The exposed stratigraphy at the DTM-[A] (**Fig. 1**) consists of an uppermost fine layer (Layer A-1) that is 46 m thick with a very coarse layer beneath (Layer A-2) that is 18 m thick. Layer A-2 appears to be slightly darker than the other layers. A coarse layer (Layer A-3) can be observed beneath these layers in the crater. In our analyses, we assumed that the radar reflection is from the interface between Layer A-2 and Layer A-3 (depth: 64 m) as this is the most plausible assumption from the estimated dielectric constants. As the subsurface reflector **(e)** in **Fig. 3** that is closest (85 km) to DTM-[A] has a delay time of 985 ns (apparent depth: 296 m), the plausible dielectric constant is estimated as 5.3 (**Fig. 4C**). Considering the error in the results for the depth/thickness of the DTM is ±5 m (cf. Noguchi et al., 2020), the plausible dielectric constant ranges from 4.6 to 6.3. We used these results for a component calculation and generated a ternary contour diagram. The value of 5.3 is consistent with the 28% porosity for a rock-air mixture and a rock-air-ice mixture of water ice contents ranging from 0 to 43% (**Fig. 4D**).

On the other hand, the exposed stratigraphy at DTM-[B] (**Fig. 1**) indicates that the uppermost coarse layer (Layer B-1) is 36 m thick while the subsurface coarse layer (Layer B-2) is only 20 m in thickness. A fine layer (Layer B-3) was observed beneath these layers deeper in the crater. Again, we assumed that the radar reflector came from the interface between Layer B-2 and Layer B-3 (depth: 56 m). Since the delay time of the subsurface reflector **(f)** in **Fig. 3** which is closest (90 km) to DTM-[B] is 907 ns (apparent depth: 272 m), the plausible dielectric constant is estimated as 5.9 (within the range 5.0 to 7.1, considering an error in the depth/thickness of ± 5 m) (**Fig. 4G**). The value 5.9 is consistent with the 25 % porosity for a rock-air mixture and up to 50 % of the volume fraction of water ice for a rock-air-ice mixture (**Fig. 4H**).

Figure 2. Distribution of subsurface reflectors in the CAP regions identified by SHARAD data overlapped with (A) a geologic map (Rotto and Tanaka, 1995) and (B) MOLA elevation data.

Colored circles show the locations of the identified subsurface reflectors, with information about their delay times. Colored squares show the locations of the RSL sites with information about their properties (Stillman et al., 2017). White arrows show the subsurface reflectors that are located near the mouths of the outflow channels. White solid lines show the nadir tracks of the SHARAD observations. Interpretations about the geological units are shown in **Text S1** of the Supporting Information.

Figure 3. Map of the AOI with the geological units. Green stars show the locations of DTM-[A] and DTM-[B]. Colored circles show the locations of nine subsurface reflectors with their delay times. **(b)-1** and **(b)-2** are on the same SHARAD orbit. DTM-[C] in **Text S2** is at 34.1°N, -43.0°E, which is close to **(a)**.

Figure 4. Radargrams for DTM-[A] and DTM-[B] on SHARAD track ID #01845801 and #02505101, respectively. (A) and (E) are the observed radargrams. The black arrows are the locations of the reflector **(e)** and **(f)** in **Fig. 3**, respectively. (B) and (F) show the simulated radargrams. (C) and (G) are estimations of the dielectric constants (red line) with the stratigraphic information shown in **Fig. 1**. (D) and (H) are ternary contour diagrams of the bulk dielectric constant for a mixture of rock, air, and water ice. The red line illustrates a dielectric constant of approximately 5.3 and 5.9, respectively. The gray triangular zone indicates the implausible porosities at the depth to the identified subsurface layer. The blue triangular zone shows the pore-filling ice parameter space.

4 Discussion

In this study, we attempted to survey the two-dimensional distribution of the shallow subsurface reflectors in the CAP regions and correlate the locations of reflectors with geological units.

More than 10^5 km^2 of reflective features in the northern plains have been detected by SHARAD (e.g., Arcadia Planitia [Bramson et al., 2015] and Utopia Planitia [Stuurman et al., 2016]). However, our study suggested that there are no such wide shallow subsurface reflectors at depths of less than 100 m in the CAP regions. One plausible explanation for the lack of wide horizontal structures is the degradation associated with the formation of outflow channels.

However, as shown in **Fig. 2**, subsurface reflectors were found at 22 scattered locations. We identified 7 locations of subsurface reflectors, which generally appeared to be near the mouths of the outflow channels (**Fig. 2**). Geologically, Rotto and Tanaka (1995) interpreted the region around a mouth (e.g. Kasei Valles, Ares Valles) as the boundary between the channel floor and the lacustrine deposits, which suggests that the 7 reflectors represent the subsurface boundaries of such geological units.

Our original motivation for this study was to search for subsurface characteristics that are related to the RSL abundant in the CAP regions. However, we did not observe any features that could be linked to the RSL sites in shallow subsurface regions such as the VM area (Noguchi et al., 2020) and we could not conclude whether the origins of RSL are wet or not. Even if CAP RSL are formed by the wet processes resulting from the presence of deep taliks (e.g. 750 m depth in the VM and SML regions) via faults such as those proposed by Abotalib and Heggy (2019), SHARAD has no capability of assessing such scenarios directly. In order to examine the relationship between the radial and concentric faults and the CAP RSL, we attempted to search

for faults in the HiRISE images of 11 craters in CAP that include RSL (red squares in **Fig. 2**). However, some of the inner walls and the surfaces near the craters were covered by dust and SHARAD can only reach depths of several hundred meters (Seu et al., 2007). We therefore could not directly discount the deep taliks hypothesis.

This study also tried to constrain the bulk porosity of the uppermost layer via combination with the DTMs generated at two locations. According to Morris and Johnson (1967), the porosities of basalt and till (regarding particle size as sand) are 17 % and 31 %, respectively. The bulk porosities of 25% and 28 % derived in this study do not contradict these values. The shallow subsurface layers that lie above the subsurface reflectors might be explained by the emplacements of basaltic rock or till. Martinez-Alonso et al. (2011) indicated evidence for glacial and volcanic activity in CAP by observing the mesas that may be analogous to terrestrial tuyas. This also suggests that complexes of basaltic rock and till may have been deposited in the CAP regions.

The real dielectric constant for this area estimated by MARSIS lies between 4.0 and 9.0 (Mouginot et al., 2012). According to Morgan et al. (2020), the ice-consistency in the upper 5 m of the CAP regions is estimated to be low (i.e., high rock-consistency). These studies suggest that shallow subsurface of CAP consists of rocky materials and our result supports the suggestion that the volume fraction of water ice is less than 50 %, indicating that the shallow subsurface of the CAP regions consists of rocky materials rather than pure water ice.

The water ice on Mars has been traced by several remote sensing techniques and numerical models. Rampart craters, which are commonly interpreted as indicating ground ice (Carr et al., 1977), suggest the presence of stable icy layers. A shallow volatile layer that was found by surveying rampart craters in Chryse Planitia has a depth range of 20–60 m (Demura and Kurita, 1998). The CAP regions are known to have maintained a volatile ice layer that was generated by outflow channels or oceans in the past. Our study indicates that the subsurface reflectors are located near the rampart craters (the closest distance was 15 km), implying that remnants of the volatile ice layer are still deposited under the CAP regions. Salvatore et al. (2010) used the Compact Reconnaissance Imaging Spectrometer for Mars (CRISM) to reveal that there was a shallow obscuration layer lying above the Hesperian basalt by observing craters in the CAP regions. The surficial obscuration material is likely multifaceted and includes the deposition of latitude-dependent mantle (LDM), which is related to the precipitation of ice and dust from the atmosphere. Orgel et al. (2019) indicated that the LDM occurred ubiquitously from 44°N to 78°N in Acidalia Planitia. Thus, the possibility that remnant ice is still present within the porous surface layer cannot be denied.

Jakosky and Carr (1985) calculated that a 2 km thick layer of ice could have been removed from the poles under a Martian obliquity of 45°. This would result in a 40 m-thick layer of ice at ±45° in the low-mid latitude regions if it were uniformly deposited (Martinez-Alonso et al., 2011). Ice may have been preferentially deposited in the CAP regions because of the high thermal inertia in these areas (Mischna et al., 2003; Schorghofer and Aharonson, 2005). Martinez-Alonso et al. (2011) suggested that it is possible that an ice-sheet reaching a few hundred-meters thick accumulated in parts of CAP because the thickness of the local ice varies according to atmospheric circulation patterns (Richardson and Wilson, 2002), thermal inertia, and topography (Mischna et al., 2003). The volume fraction of water ice in a rock-air-ice mixture derived in this study was less than 50 %. Thus, if local ice that was carried from the poles is still present, water ice would be preserved as ice-cemented regolith, not pure water ice.

5 Conclusions

A survey of the subsurface structure of CAP was carried out using MRO SHARAD data and several locations were identified where subsurface reflectors are distributed. No wide areas of subsurface materials with large permittivity contrast were observed. The scattered distribution of the subsurface reflectors was correlated with geological units; however, no links with the RSL sites were found.

We then used the delay time in the radar data and the plausible depth of the stratigraphic exposure on the crater walls to constrain the bulk dielectric constants of the uppermost layers in two locations. The estimated values of 5.3 and 5.9 suggest bulk porosities of 28 % and 25 % for basaltic rocks and till, respectively. The bulk dielectric constants suggested upper limits of approximately 43 % and 50 % for the volume fraction of water ice. This large porosity may indicate that the subsurface layers can include pore-filling ice such as ice-cemented regolith if local ice that was carried from the poles is still present.

Acknowledgments

We used the data from SHARAD on the Planetary Data System and HiRISE on the website of the University of Arizona (https://hirise.lpl.arizona.edu/) with HiView (https://www.uahirise.org/hiview/). The HiRISE DTMs were processed using the MarsSI (https://marssi.univ-lyon1.fr/MarsSI/) application with the support of Matthieu Volat. This work is supported by a Grant-in-Aid for Scientific Research (19H00707 and 17H06459) from the Japan Society for the Promotion of Science.

References

Abotalib, A.Z., E. Heggy (2019), A deep groundwater origin for recurring slope lineae on Mars. *Nature Geosci.*, 12, 235-241. https://doi.org/10.1038/s41561-019-0327-5

Baker, V.R. R.G. Strom, V.C. Gulick, J.S. Kargel, G. Komatsu, V. S. Kale (1991), Ancient oceans, ice sheets and hydrological cycle on Mars. *Nature*, 352, 589-594. https://doi.org/10.1038/352589a0

Bramson, A.M., S. Byrne, N.E. Putzig, S. Sutton, J.J. Plaut, T.C. Brothers, J.W. Holt (2015), Widespread excess ice in Arcadia Planitia, Mars. *Geophys. Res. Lett.*, 42, 6566-6574. https://doi.org/10.1002/2015GL064844

Campbell, M.J. and J. Ulrichs (1969), Electrical properties of rocks and their significance for lunar radar observations. *J. Geophys. Res.*, 74(25), 5867-5881. https://doi.org/10.1029/JB074i025p05867

Carr, M.H., L.S. Crumpler, J.A. Cutts, R. Greeley, J.E. Guest, H. Masursky (1977), Martian impact craters and emplacement of ejecta by surface flow. *J. Geophys. Res.*, 82, 4055-4065. https://doi.org/10.1029/JS082i028p04055

Carr, M.H. (1996), Channels and valleys on Mars: Cold climate features formed as a result of a thickening cryosphere. *Planet. Space Sci.*, 44, 1411-1423. https://doi.org/10.1016/S0032-0633(96)00053-0

313 Clifford, S.M., T.J. Parker (2001), The evolution of the Martian hydrosphere: Implications for
314 the fate of a primordial Martian ocean and current state of the northern plains. *Icarus*, 154, 40-
315 79. https://doi.org/10.1006/icar.2001.6671

316 Costard, F., F. Forget, N. Mangold, J.P. Peulvast (2002), Formation of recent Martian debris
317 flows by melting of near-surface ground ice at high obliquity. *Science*, 295, 110-113,
318 https://doi.org/10.1126/science.1066698

319 Demura, H., K. Kurita (1998), A shallow volatile layer at Chryse Planitia, Mars. *Earth Planets*
320 *Space*, 50, 423-429. https://doi.org/10.1186/BF03352129

321 Dundas, C.M., et al. (2018), Exposed subsurface ice sheets in Martian mid-latitudes. *Science*,
322 359, 199–201. https://doi.org/10.1126/science.aao1619

323 Head, J.W., M.A. Kreslavsky, S. Prattet (2002), Northern lowlands of Mars: Evidence for
324 widespread volcanic flooding and tectonic deformation in the Hesperian Period. *J. Geophys.*
325 *Res.*, 107, E15003. https://doi.org/10.1029/2000JE001445

326 Hoffman, N. (2000), White Mars: A new model for Mars' surface and atmosphere based on CO_2.
327 *Icarus*, 146, 326-342. https://doi.org/10.1006/icar.2000.6398

328 Huber, C., L. Ojha, L. Lark, J.W. Heada (2020), Physical models and predictions for recurring
329 slope lineae formed by wet and dry processes. *Icarus*, 335, 113385.
330 https://doi.org/10.1016/j.icarus.2019.07.019

331 Ishiyama, K., A. Kumamoto, Y. Takagi, N. Nakamura, S. Hasegawa (2019), Effect of crack
332 direction around laboratory-scale craters on material bulk permittivity. *Icarus*, 319, 512–524.
333 https://doi.org/10.1016/j.icarus.2018.09.030

334 Jakosky, B.M., M.A. Carr (1985), Possible precipitation of ice at low latitudes of Mars during
335 periods of high obliquity. *Nature*, 315, 559-561. https://doi.org/10.1038/315559a0

336 Kreslavsky, M.A., J.W. Head (2002), Fate of outflow channel effluents in the northern lowlands
337 of Mars: The Vastitas Borealis Formation as a sublimation residue from frozen ponded bodies of
338 water. *J. Geophys. Res.*, 107, E125121. https://doi.org/10.1029/2001JE001831

339 Leverington, D.W. (2011), A volcanic origin for the outflow channels of Mars: Key evidence
340 and major implications, *Geomorphology*, 132, 51-75,
341 https://doi.org/10.1016/j.geomorph.2011.05.022

342 McEwen, A.S., et al. (2007), Mars Reconnaissance Orbiter's High Resolution Imaging Science
343 Experiment (HiRISE). *J. Geophys. Res.*, 112, E05S02. https://doi.org/10.1029/2005JE002605

344 Martinez-Alonso, S., M.T. Mellon, M.E. Banks, L.P. Keszthelyi, A.S.McEwen, The HiRISE
345 Team (2011), Evidence of volcanic and glacial activity in Chryse and Acidalia Planitiae, Mars.
346 *Icarus*, 212, 597-621. https://doi.org/10.1016/j.icarus.2011.01.004

347 Matsuoka, T., S. Fujita, S. Mae (1997), Dielectric properties of ice containing ionic impurities at
348 microwave frequencies. *J. Phys. Chem.*, 101, 6219-6222. https://doi.org/10.1021/jp9631590

349 Mischna, M.A., M.I. Richardson, R.J. Wilson, D.J. McCleese (2003), On the orbital forcing of
350 Martian water and CO_2 cycles: A general circulation model study with simplified volatile
351 schemes. *J. Geophys. Res.*, 108, E6, 5062. https://doi.org/10.1029/2003JE002051

Morgan, N.E., et al. (2020), Subsurface Water Ice Mapping (SWIM) on Mars: Radar surface reflectivity. The 51st Lunar Planet. Sci. Conf., LPI Contribution No. 2326, 2020, id.2790. https://www.hou.usra.edu/meetings/lpsc2020/pdf/2790.pdf

Morris, D.A., A.I. Johnson (1967), Summary of hydrologic and physical properties of rock and soil materials, as analyzed by hydrologic laboratory of the U.S. Geological Survey 1948-1960. *U.S. Geol. Surv. Water Supply Pap.*, 1839-D. https://doi.org/10.3133/wsp1839D

Mouginot, J., A. Pommerol, P. Beck, W. Kofman, S.M. Clifford (2012), Dielectric map of the Martian northern hemisphere and the nature of plain filling materials. *Geophys. Res. Lett.*, 39, L02202. https://doi.org/10.1029/2011GL050286

Mustard, J.F., et al. (2001), Evidence for recent climate change on Mars from the identification of youthful near-surface ground ice, *Nature*, 412, 411–414. https://doi.org/10.1038/35086515

Noguchi, R., K. Ishiyama, A, Kumamoto, C. Uemura, Y. Kasaba, T. Usui, A. Oura, D. Shoji (2020), Radar sounding of subsurface structure in eastern Coprates and Capri Chasmata, Mars. Geophys. Res. Lett., 47, 16, e2020GL088556, https://doi.org/10.1029/2020GL088556

Orgel, C., et al. (2019), Grid mapping the northern plains of Mars: A new overview of recent water- and ice-related landforms in Acidalia Planitia. *J. Geophys. Res.*, 124, 454-482. https://doi.org/doi:10.1029/2018JE005664

Pacifici, A., G. Komatsu, M. Pondrelli (2009), Geological evolution of Ares Vallis on Mars: Formation by multiple events of catastrophic flooding, glacial and periglacial processes. *Icarus*, 45, 77-86. https://doi.org/10.1016/j.icarus.2009.02.029

Putzig, N.E., R.J. Phillips, B.A. Campbell, M.T. Mellon, J.W. Holt, T.C. Brothers (2014), SHARAD soundings and surface roughness at past, present, and proposed landing sites on Mars: Reflections at Phoenix may be attributable to deep ground ice. *J. Geophys. Res.*, 119, 1936-1949. https://doi.org/10.1002/2014JE004646

Quantin-Nataf, C., et al. (2018), MarsSI: Martian surface data processing information system. *Planet. Space Sci.*, 150, 157-170. https://doi.org/10.1016/j.pss.2017.09.014

Richardson, M.I., R.J. Wilson (2002), Investigation of the nature and stability of the Martian seasonal water cycle with a general circulation model. *J. Geophys. Res.*, 107, 5031. https://doi.org/10.1029/2001JE001536

Rodoriguez, J.A.P., et al. (2006), Headward growth of chasmata by volatile outbursts, collapse, and drainage: Evidence from Ganges chaos, Mars. *Geophys. Res. Lett.*, 33, L18203. https://doi.org/10.1029/2006GL026275

Rodoriguez, J.A.P., et al. (2014), Evidence for Middle Amazonian catastrophic flooding and glaciation on Mars. *Icarus*, 242, 202-210. https://doi.org/10.1016/j.icarus.2014.06.008

Rotto, S., K.L. Tanaka (1995), Geologic/geomorphic map of the Chryse Planitia region of Mars. *U.S. Geol. Surv. Misc. Invest. Ser.*, Map 1-2441, scale 1:5M. https://doi.org/10.3133/i2441

Rust, A.C., J.K. Russell, R.J. Knight (1999), Dielectric constant as a predictor of porosity in dry volcanic rocks. *J. Volcanol. Geotherm. Res.*, 91, 79-96. https://doi.org/10.1016/S0377-0273(99)00055-4

391 Salvatore, M.R., J.F. Mustard, M.B. Wyatt, S.L. Murchie (2010), Definitive evidence of
392 Hesperian basalt in Acidalia and Chryse Planitiae. *J. Geophys. Res*., 115, E07005,
393 https://doi.org/10.1029/2009JE003519

394 Schorghofer, N., O. Aharonson (2005), Stability and exchange of subsurface ice on Mars. *J.*
395 *Geophys. Res.*, 110, E05003. https://doi.org/10.1029/2004JE002350

396 Seu, R., et al. (2007), SHARAD sounding radar on the Mars Reconnaissance Orbiter. *J.*
397 *Geophys. Res*., 112, E05S05. https://doi.org/10.1029/2006JE002745

398 Smith, D.E., et al. (2001), Mars Orbiter Laser Altimeter: Experiment summary after the first year
399 of global mapping of Mars. *J. Geophys. Res.*, 106, 23689–23722,
400 https://doi.org/10.1029/2000JE001364

401 Stillman, D.E., T.I. Michaels, R.E. Grimm, J. Hanley (2016), Observations and modeling of
402 northern mid-latitude recurring slope lineae (RSL) suggest recharge by a present-day martian
403 briny aquifer. *Icarus*, 265, 125-138. https://doi.org/10.1016/j.icarus.2015.10.007

404 Stillman, D.E., T.I. Michaels, R.E. Grimm (2017), Characteristics of the numerous and
405 widespread recurring slope lineae (RSL) in Valles Marineris, Mars. *Icarus*, 285, 195-210.
406 https://doi.org/10.1016/j.icarus.2016.10.025

407 Stuurman, C.M., G.R. Osinski, J.W. Holt, J.S. Levy, T. Brothers, M. Kerrigan, B.A. Campbell
408 (2016), SHARAD detection and characterization of subsurface water ice deposits in Utopia
409 Planitia, Mars. *Geophys. Res. Lett.*, 43, 9484-9491. https://doi.org/10.1002/2016GL070138

410 Tanaka, K.L. (1999), Debris-flow origin for the Simud/Tiu deposit on Mars. *J. Geophys. Res*.,
411 104, 8637-8652. https://doi.org/10.1029/98JE02552

Figure 1.

A

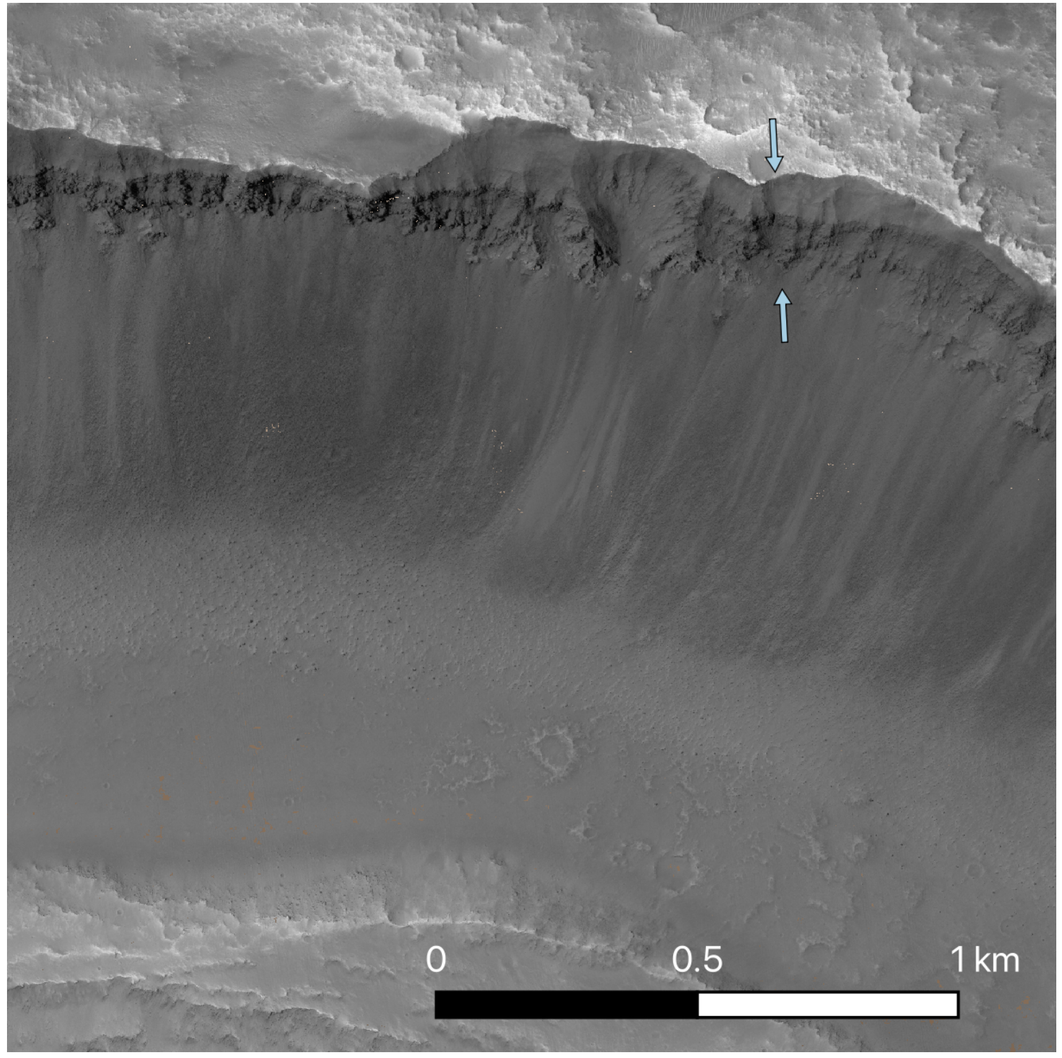

B

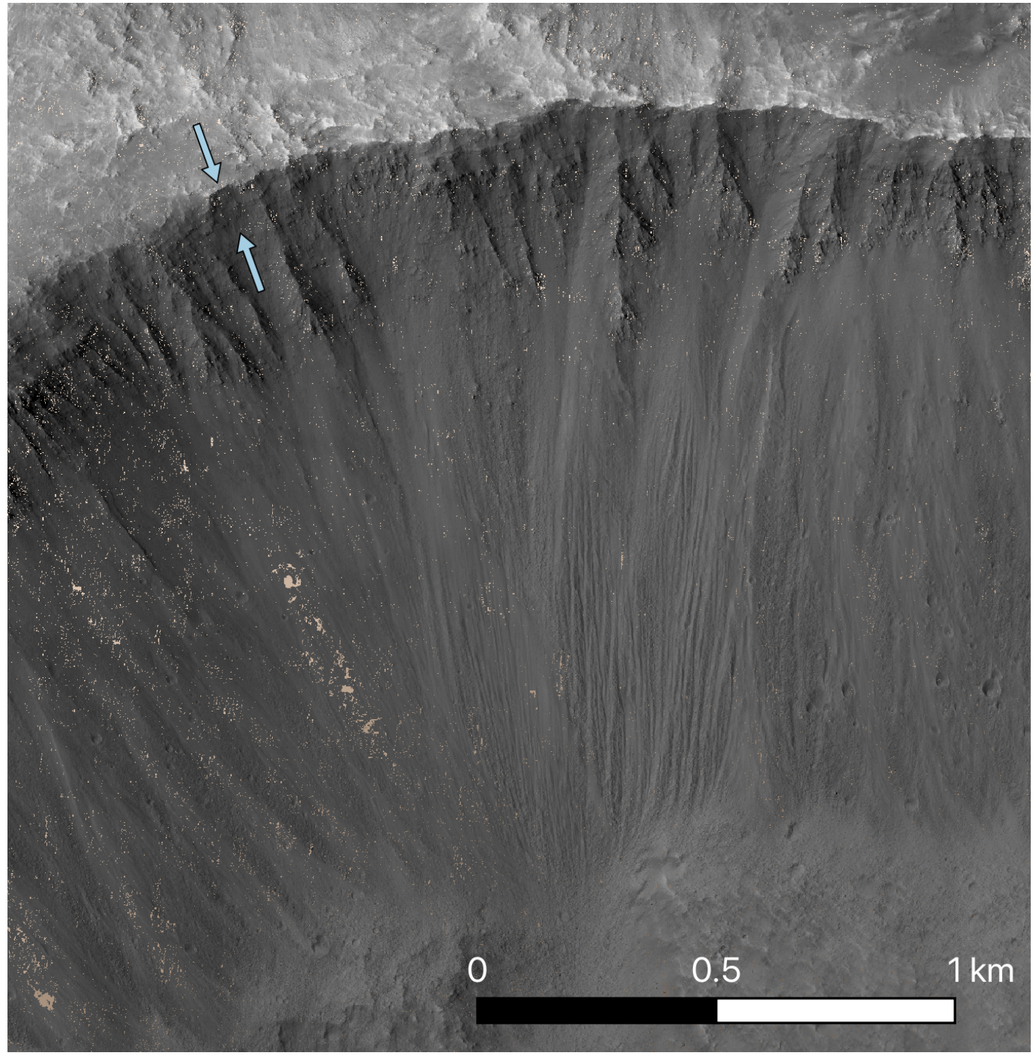

C

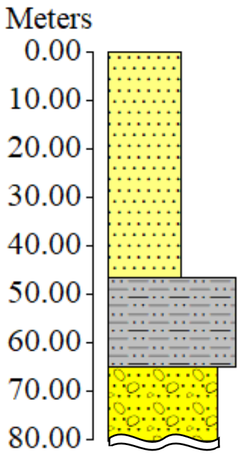

Fine layer	: Layer A-1
Very coarse layer	: Layer A-2
Coarse layer	: Layer A-3

D

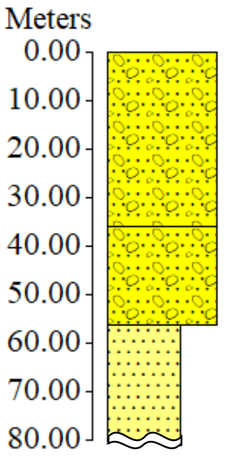

Coarse layer	: Layer B-1
Coarse layer	: Layer B-2
Fine layer	: Layer B-3

Figure 2.

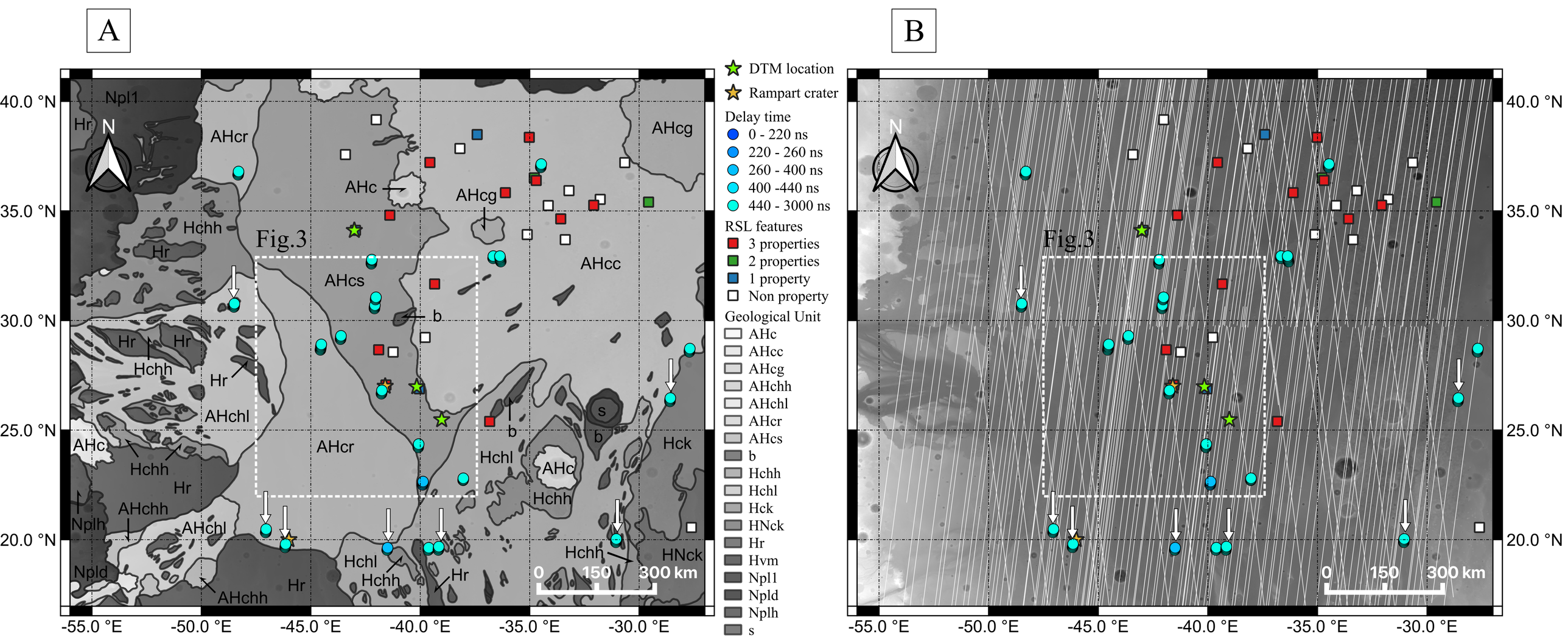
A
B
Fig.3
Fig.3
N
N
DTM location
Rampart crater
Delay time
0 - 220 ns
220 - 260 ns
260 - 400 ns
400 -440 ns
440 - 3000 ns
RSL features
3 properties
2 properties
1 property
Non property
Geological Unit
AHc
AHcc
AHcg
AHchh
AHchl
AHcr
AHcs
b
Hchh
Hchl
Hck
HNck
Hr
Hvm
Npl1
Npld
Nplh
s
Npl1
Hr
AHcr
AHc
AHcg
Hchh
Hr
AHcc
AHcs
b
Hr
Hr
Hchh
Hr
AHchl
AHc
Hchh
Hr
AHchh
Nplh
AHchl
Npld
AHchh
Hr
Hchl
Hchh
Hr
AHcr
Hchl
AHc
Hchh
s
b
Hck
Hchh
HNck
0
150
300 km
0
150
300 km
40.0 °N
35.0 °N
30.0 °N
25.0 °N
20.0 °N
-55.0 °E
-50.0 °E
-45.0 °E
-40.0 °E
-35.0 °E
-30.0 °E

Figure 3.

track ID: 03105101
delay time: 959 ns
(a)
track ID: 04915601
delay time: 1761 ns
(b)-1
(b)-2
track ID: 04915601
delay time: 730 ns
b
track ID: 00446802
delay time: 889 ns
(c)
(d)
track ID: 00411201
delay time: 769 ns
(e)
track ID: 01845801
delay time: 985 ns
track ID: 02505101
delay time: 907 ns
(f)
track ID: 03814501
delay time: 831 ns
(g)
track ID: 04923501
delay time: 367 ns
(h)
Hr
AHchl
AHcc
AHcs
AHcr
Hchl
Hchh
A
B
0 50 100 km
32.5 °N
30.0 °N
27.5 °N
25.0 °N
22.5 °N
-47.5 °E
-45.0 °E
-42.5 °E
-40.0 °E
-37.5 °E
DTM location
Rampart crater
Delay time
0 - 220 ns
220 - 260 ns
260 - 400 ns
400 -440 ns
440 - 3000 ns
RSL feature
3 properties
2 properties
1 property
Non property
Geological Unit
AHcc
AHchl
AHcr
AHcs
b
Hchh
Hchl
Hr

Figure 4.

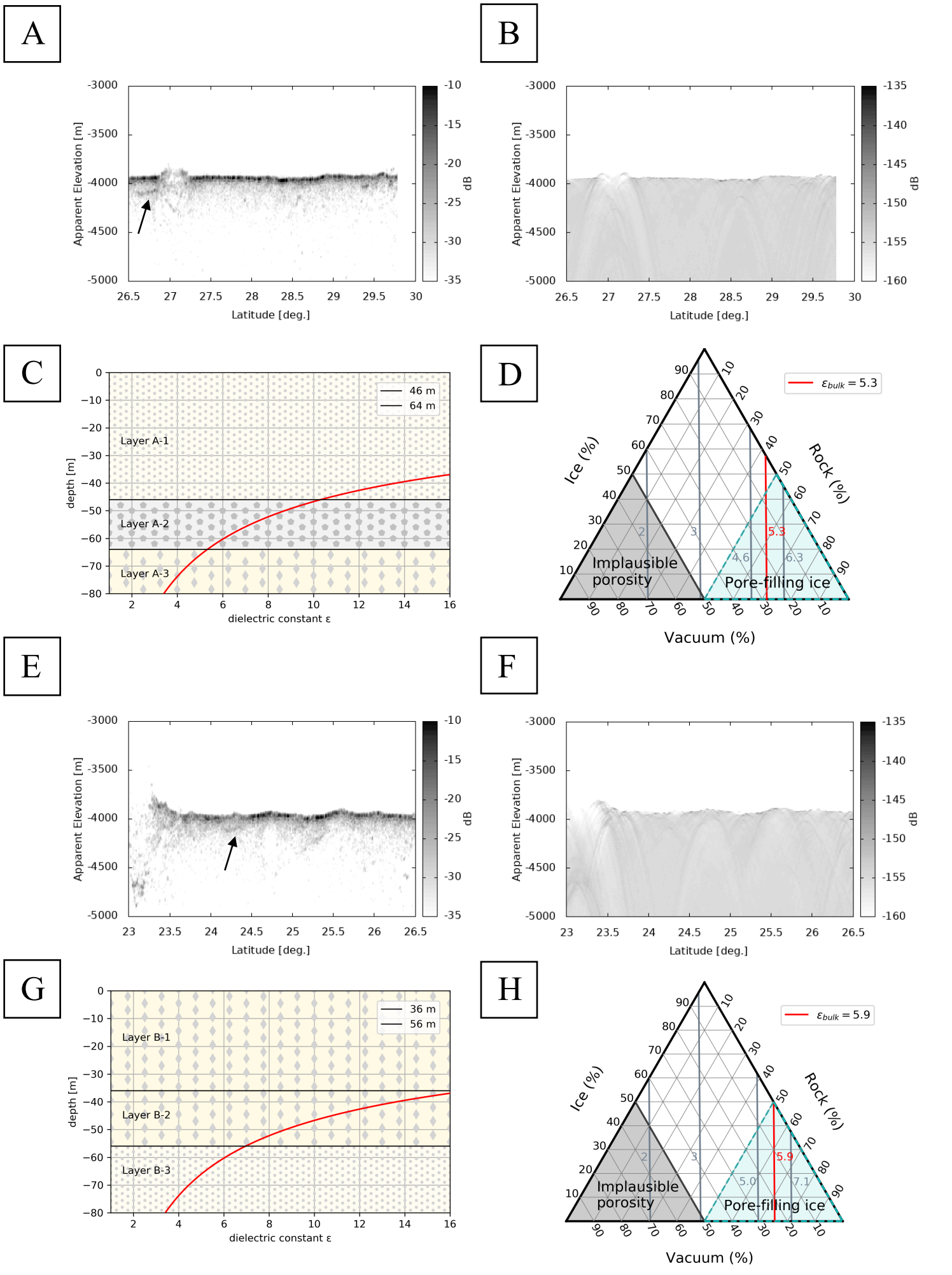
A
B
C
D
E
F
G
H
Apparent Elevation [m]
Latitude [deg.]
dB
depth [m]
dielectric constant ε
46 m
64 m
Layer A-1
Layer A-2
Layer A-3
36 m
56 m
Layer B-1
Layer B-2
Layer B-3
$\varepsilon_{bulk} = 5.3$
$\varepsilon_{bulk} = 5.9$
Ice (%)
Rock (%)
Vacuum (%)
Implausible porosity
Pore-filling ice